OPTICS

A *Janus* emitter for passive heat release from enclosures

Se-Yeon Heo[1]*, Gil Ju Lee[1]*, Do Hyeon Kim[1], Yeong Jae Kim[1], Satoshi Ishii[2,3], Min Seok Kim[1], Tae Joon Seok[1], Bong Jae Lee[4], Heon Lee[5], Young Min Song[1]†

Passive radiative cooling functions by reflecting the solar spectrum and emitting infrared waves in broadband or selectively. However, cooling enclosed spaces that trap heat by greenhouse effect remains a challenge. We present a *Janus* emitter (*J*ET) consisting of an Ag–polydimethylsiloxane layer on micropatterned quartz substrate. The induced spoof surface plasmon polariton helps overcome inherent emissivity loss of the polymer and creates near-ideal selective and broadband emission on the separate sides. This design results in not only remarkable surface cooling when the *J*ET is attached with either side facing outwards but also space cooling when used as an enclosure wall. Thus, the *J*ET can passively mitigate the greenhouse effect in enclosures while offering surface cooling performance comparable to conventional radiative coolers.

INTRODUCTION

Current cooling technologies mostly rely on vapor compression and fluid-cooled systems (1). However, they consume ~10% of the global energy and accelerate the depletion of fossil fuels (2, 3). Moreover, CO_2 emissions from space cooling have more than tripled between 1990 and 2018 to reach 1130 million tons, and other environmental issues such as ozone depletion and air pollution are worsening (3). Radiative cooling, which is how the Earth cools itself, is a passive thermal management strategy (4). Using the spectral overlap between the peak in Planck's blackbody radiation at ~300 K and the atmospheric transmission window between 8 and 13 μm, unwanted heat can be emitted to outer space without energy consumption or pollutant emission (5, 6).

Recently, reported passive radiative coolers have demonstrated subambient cooling during the daytime (7–14). Those coolers are attached on exterior materials, roof, or human skin to draw heat from the periphery through conduction and convection (15–17). However, this cooling becomes insufficient when heat extremely accumulates continuously in an enclosed space, such as stationary vehicles in daytime (conventional cooler; fig. S1A) (18, 19). This is because the conventional radiative cooler (C-RC) only considers emissivity of the side exposed to the sky (20–25), although the inner side also notably affects cooling in enclosures by radiation-convection interaction (26). In particular, very high temperatures can develop under the greenhouse effect, when the windows are transparent to solar radiation coming in but opaque to the long-wave thermal radiation going out (18, 19). However, emissivity on the inner side could allow the trapped heat to escape by increasing the inner radiation flux, which is maximized by combining natural convection. Accordingly, strategic design of emission spectra on both sides of the cooler is vital for releasing the trapped heat.

[1]School of Electrical Engineering and Computer Science (EECS), Gwangju Institute of Science and Technology, 123 Cheomdangwagi-ro, Buk-gu, Gwangju 61005, Republic of Korea. [2]International Center for Materials Nanoarchitectonics, National Institute of Materials Science (NIMS), 1-1 Namiki, Tsukuba, Ibaraki 305-0044, Japan. [3]Japan Science and Technology Agency, PRESTO, 4-1-8 Honcho, Kawaguchi, Saitama 332-0012, Japan. [4]Department of Mechanical Engineering, Korea Advanced Institute of Science and Technology (KAIST), 291 Daehak-ro, Yuseong-gu, Daejeon 34141, Republic of Korea. [5]Department of Materials Science and Engineering, Korea University, 145 Anam-ro, Sungbuk-gu, Seoul 02841, Republic of Korea.
*These authors contributed equally to this work.
†Corresponding author. Email: ymsong@gist.ac.kr

Here, we propose a *Janus* thermal emitter that acts as a selective emitter (SE) on the top side and a broadband emitter (BE) on the bottom side. This design effectively draws heat from the inner space as well as the surface, because the bottom side can absorb thermal input in a broad spectral range, while the top side emits heat to space without disturbing ambient radiation (*Janus* cooler; fig. S1B). We first designed a polymer-based SE that uses spoof surface plasmon polariton (sSPP) to achieve near-ideal selectivity, using the dispersion relation of sSPP and three-dimensional optical simulations. Next, we theoretically and experimentally demonstrate the remarkable surface cooling performances of the *Janus* emitter (*J*ET) on both sides, which is a traditional attribute of the state-of-the-art radiative coolers (table S1). Last, the *J*ET was used to replace a wall of an airtight space, with the SE side facing outward. Compared to the C-RC, it sustained a larger temperature drop in the enclosure material. These approaches are useful in developing advanced passive cooling techniques that work simultaneously for the surface and space.

RESULTS AND DISCUSSION

JET for cooling enclosed space

Solar radiation through the window can significantly heat the interior of a stationary automobile. The *J*ET can function as an effective heat channel by using its bottom side to absorb broadband thermal radiation from the interior and its top side to radiate heat as infrared (IR) waves to the outer space as a cold sink (Fig. 1A). The fabricated sample (Fig. 1B) comprises a 4-μm-thick polydimethylsiloxane (PDMS) layer, 100-nm-thick silver layer, and 500-μm-thick micropatterned quartz layer coated with 10-μm-thick PDMS on the bottom side. Ideally, the top side of the *J*ET needs to display selective emission matching the atmospheric window to minimize the disturbance from solar energy and ambient radiation (Fig. 1C, top). Moreover, the idealized bottom side should broadly absorb inner thermal radiation (Fig. 1C, bottom).

The Ag layer mostly reflects the solar spectrum and isolates the top and bottom sides in the far-IR (FIR) region, enabling the *J*ET to function in the SE and BE (Fig. 1D). The Ag-PDMS groove causes sSPP resonance, which helps the PDMS thin film to overcome the intrinsic emissivity loss due to the material's abnormal extinction coefficient (Fig. 1E, top and middle; see table S2 for the origins of localized strong absorption peaks in the thin PDMS film). In principle, the easiest way to compensate for the emissivity loss is to use
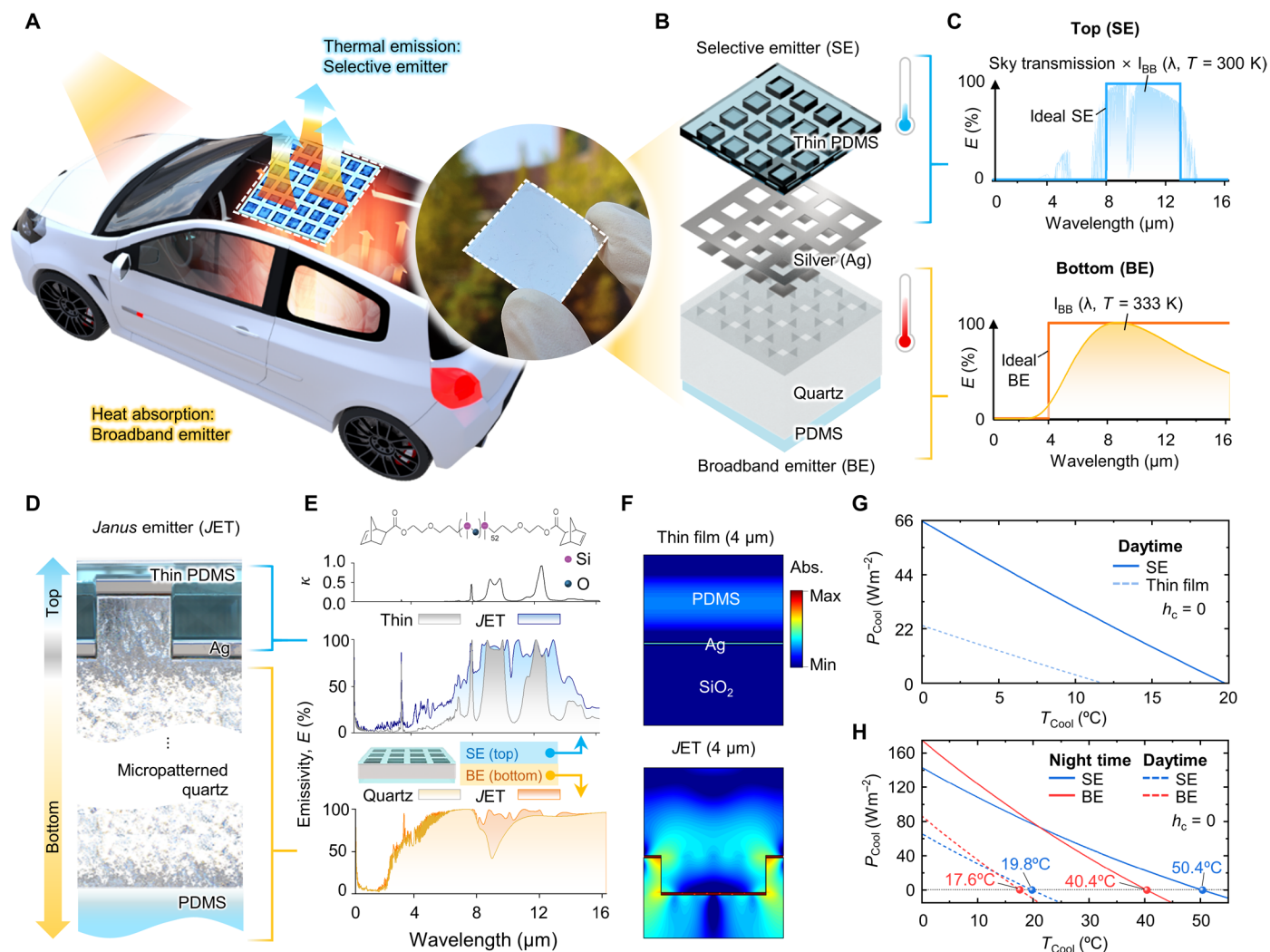
Fig. 1. JET for cooling enclosed space. (**A**) Schematic of JET applied to a stationary automobile under direct sunlight, where heat is trapped by the greenhouse effect. The *Janus* thermal radiation property allows broadband absorption of IR waves from the enclosure and selective emission to the ultracold space. Inset photograph: Fabricated JET exhibiting strong reflection in the visible range. Photo credit: Yeong Jae Kim, GIST. (**B**) Magnified structural view. From top to bottom: 4-μm PDMS, silver, micropatterned quartz, and 10-μm PDMS. (**C**) Emission spectra of the ideal JET with broadband emission (BE) on the bottom and selective emission (SE) on the top. BB, blackbody radiation. (**D**) Cross-sectional schematic view of JET. (**E**) Top: Polymer structure and extinction coefficient of PDMS. Simulated FIR emission spectra of JET for the SE (middle) and BE (bottom) in the 0- to 16-μm wavelength region. (**F**) Absorption profiles of thin PDMS (top) and JET (bottom) at 10.75-μm wavelength, where the largest emission loss occurs in thin PDMS. (**G** and **H**) Calculated cooling powers (P_{cool}) and cooling temperatures (T_{cool}) under AM1.5G solar radiation for (G) PDMS thin film versus SE in daytime and (H) SE versus BE in daytime (dashed lines) and nighttime (solid lines).

thicker polymer films; however, this inevitably broadens the emission spectrum (fig. S2) (*9*, *12*, *27–32*). In contrast, the induced sSPP resonance in the JET can realize near-ideal selective emission even with an extremely thin layer of PDMS (4 μm). Moreover, the bottom side of the JET ameliorates the emissivity dip of a sufficiently thick quartz substrate (500 μm) (Fig. 1E, bottom). Because of sSPP resonance, strong absorptions are induced at discontinuities of the Ag layer (Fig. 1F).

The cooling powers and cooling temperatures for the SE and BE were calculated using the thermal equilibrium equation, assuming a solar radiation [$I_{AM1.5}(\lambda)$] of 1000 W/m² (Fig. 1, G and H; detailed calculation in Supplementary Text). In daytime, the SE outpaces the PDMS thin film in cooling power (P_{Cool}, 66 W/m²) and cooling temperature (T_{Cool}, 19.8°C), excluding convection and conduction

effects. The SE also has higher cooling temperature than the BE (10.0 and 2.2°C at night and daytime, respectively), while the BE has better cooling power (maximum: 175 W/m² during the night).

sSPP resonance for near-ideal SE
Using the dispersion equation and spectral simulations, we analyze the effects of the sSPP resonances on the emissivity of JET (Fig. 2, A to D) (*33*). Within the atmospheric window (8 to 13 μm), calculation of the sSPP wavelength is notably complex because the PDMS has abnormal dispersion. Instead, the dispersion curve and emissivity spectra of the JET were calculated using an air substrate and only the refractive index of PDMS except for absorption (extinction coefficient = 0) (Fig. 2, A and B). The structural parameters are as follows: period (p) = 8.5 μm, depth (d) = 1.7 μm, width (w) = 6.375 μm,
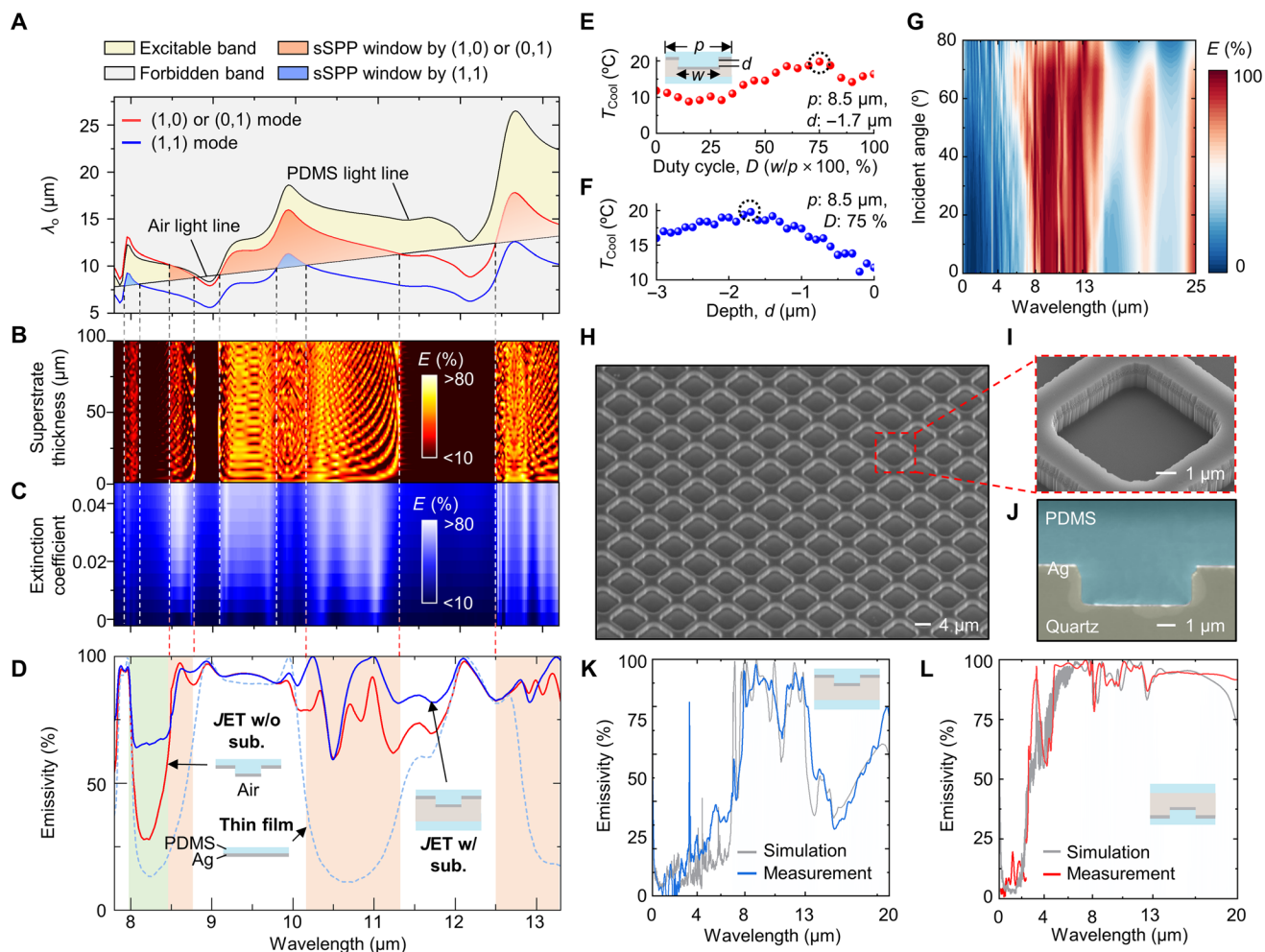
Fig. 2. Theoretical analyses, optimization, and characterization of *J*ET. (A) Dispersion curve of sSPP for the superstrate with the refractive index of PDMS. Yellow and gray shaded areas: Excitable band and forbidden band of sSPP determined by air and PDMS light lines, respectively. Orange and bluish shaded regions: sSPP windows from the (1,0)/(0,1) and (1,1) modes, respectively. **(B and C)** Emissivity spectra as a function of (B) thickness of a nonabsorbing superstrate and (C) extinction coefficient of superstrate. These results show that emission enhancements depending on the superstrate thickness and extinction coefficient only occur in sSPP windows, particularly the sSPP window from the (1,0)/(0,1) modes. **(D)** Emissivity spectra of thin-film PDMS (sky blue dashed line) and *J*ET without and with SiO_2 substrate (red and blue lines, respectively). Orange boxes: Areas with enhanced emissivity by sSPP windows. White boxes: Regions with inherently strong emissivity by PDMS owing to high extinction coefficient. Greenish box: SiO_2 substrate reinforces the emissivity dip that is uncovered by the sSPP window and strong emissivity region. **(E and F)** Optimizations of duty cycle and depth. **(G)** Calculated angular response of *J*ET, showing maintained selective emission feature up to the incident angle of 80°. **(H to J)** SEM images of optimized *J*ET (H and I) without Ag or PDMS coating and (J) with Ag and PDMS coating. **(K and L)** Measured and simulated emissivity spectra for the (K) SE and (L) BE of fabricated *J*ET.

top PDMS thickness (t) = 4 μm, and bottom PDMS thickness (h) = 10 μm (fig. S3A). The simulation result in Fig. 2B shows that strong resonant absorption peaks are excited between the two sSPP modes, which is defined as "sSPP window" in this study. These peaks are due to Fabry-Perot cavity resonance, which depends on the thickness of the superstrate. The sSPP window becomes a frame to modulate the emissivity. With a small extinction coefficient of 0.04, the emissivity loss is enhanced within the sSPP windows (Fig. 2C).

From the emissivity spectra for three layouts (thin film and *J*ET without/with SiO_2 substrate), the sSPP windows from the (1,0) or (0,1) modes could remediate emissivity loss in the PDMS thin film (Fig. 2D, orange boxes). The wavelength regions corresponding to high extinction coefficients for PDMS show strong emissivity in all layouts (Fig. 2D, white boxes). The micropatterned substrate sup-

ports the uncovered emissivity loss by the sSPP windows in the wavelength range of 8 to 8.5 μm (Fig. 2D, green box). Below 8.5 μm, diffraction occurs by the metal grating in the *J*ET, reinforcing the emissivity dip because of the Si-O-Si asymmetric stretching phonon mode in quartz (fig. S3B). Thus, by matching the sSPP windows to the atmospheric window, the inherent emissivity loss of the thin PDMS film is ameliorated. The dispersion equation of sSPP is solved in detail in Supplementary Text.

The dispersion curve can determine the optimum period of the *J*ET because the dispersion equation of sSPP is a function of a period. Other geometrical parameters were studied in terms of the cooling performance based on the calculated emissivity spectra. A silver layer of 100 nm is sufficient for reflecting the solar spectrum and separating the emissivity spectra of the top and bottom sides in *J*ET

(fig. S3, C and D). The thickness of the PDMS layer was chosen to be 4 μm to establish the selective emission feature (fig. S3E). For d and the duty cycle (D; determined by p times w), optimization calculations were performed using the simulated emissivity spectra of the JETs (Fig. 2, E and F). The optimum values are $D = 75\%$ and $d = -1.7$ μm, with a maximum cooling temperature of $-19.8°C$ for a solar irradiance of 1000 W/m² with zero nonradiative heat exchange (i.e., $h_c = 0$). Moreover, the JET shows angle-robust emissivity near the atmospheric window (Fig. 2G).

Figure 2H shows scanning electron microscopy (SEM) images of the optimum micropatterned quartz without Ag or PDMS coating (single unit cell: Fig. 2I; top and cross-sectional views: fig. S4, A and B). The fabricated JET is displayed in the cross-sectional view (Fig. 2J). According to the measured and simulated emissivity spectra, the fabricated JET has near-ideal features in both SE and BE (Fig. 2, K and L). Near-ideal BE is implemented by coating 10-μm-thick PDMS at the bottom side, based on the simulated emissivity spectra versus PDMS thickness (fig. S3F). The emissivity spectra of the bare thin-film PDMS and bare quartz are shown in fig. S4 (C and D).

Surface cooling performances of JET in SE and BE

The cooling power and cooling temperatures of the BE and SE were investigated experimentally on an outdoor rooftop at Gwangju Institute of Science and Technology (GIST; 35°13'36.5"N, 126°50'24.0"E) (Fig. 3A). Self-heating of ambient air sensor was prevented by using "ambient air box," which shades solar spectrum and provides continuous airflow (fig. S5, A and B). In addition, the temperature sensors were tested for reliability (fig. S5, C to E). A convection shield

is not used here because of its imperfect transmittance (fig. S5F). Experimental results show subambient cooling under different weather conditions of clear and haze (Fig. 3B; see fig. S5, G to I, for the details). On day 2, SE shows subambient cooling of ~6°C under peak solar power of ~680 W/m². The SE has a lower temperature of ~1°C, being lower (i.e., higher cooling temperature) than the BE. Cooling temperature of ~3.4°C was also achieved in day 4, where haze and humidity inhibit radiative heat transfer to the universe (9).

Using the measured data, the steady-state energy balance equation was decomposed in four power terms: emitted power by the sample (P_{rad}), absorbed power of the atmospheric emission (P_{atm}), absorbed power of the solar irradiation (P_{Sun}), and nonradiative heat transfer including conduction and convection ($P_{non-rad}$) (Fig. 3C). In both SE and BE, P_{Sun} and $P_{non-rad}$ are similar at all measured times. The SE is less disturbed by radiation from the atmosphere (i.e., low P_{atm}) owing to its SE feature. For efficient subambient cooling, a low P_{atm} is imperative because P_{rad} decreases when the radiative cooler becomes colder, while the level of P_{atm} is sustained as the ambient air temperature is unchanged. Therefore, the SE is more effective in subambient cooling than the BE.

Figure 3 (D to G) shows the cooling power measurement including climate conditions (Fig. 3, D and E). Two direct current (DC) power supplies turned on heaters attached on the backside of two emitters (details provided in Methods of Supplementary Text). The cooling power was defined as the power consumed by the heater to restore sample to ambient temperature (7) of the two emitters continuously monitored during 30 hours (details provided in Materials and Methods). According to Fig. 3C, the BE theoretically emits more
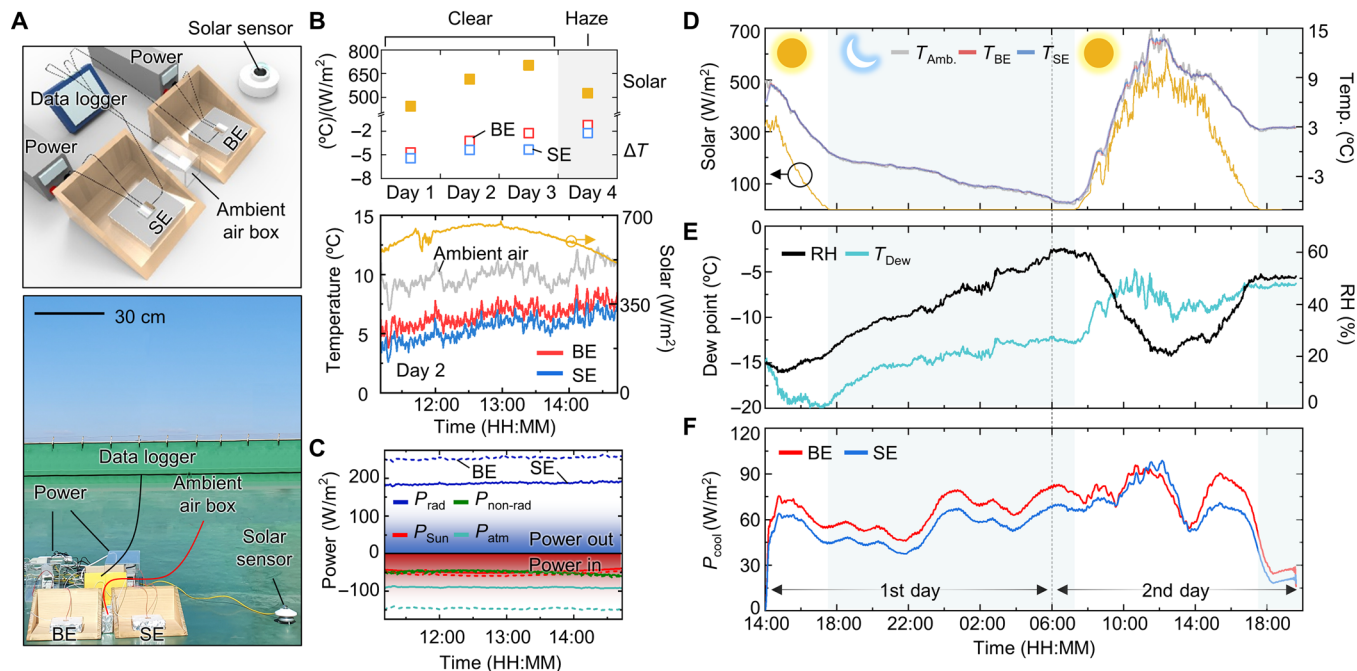

Fig. 3. Surface cooling performances of two emitters in JET. (**A**) (Top) Schematic illustration and (bottom) photograph of the radiative cooler in rooftop test configuration. Ambient air box, which prevents self-heating of air sensor, is shown in fig. S5 (A and B) in detail. Photo credit: Gil Ju Lee, GIST. (**B**) (Top) Average solar intensity and average cooling temperature (ΔT) of SE and BE in clear and haze days. All data demonstrate that SE has better subambient cooling performance. (Bottom) Detailed logged temperature measured of the result for day 2. (**C**) Calculated power components in the thermal equilibrium equation (P_{rad}, P_{Sun}, $P_{non-rad}$, and P_{atm}) over time, using data in (B). The dashed line indicates BE, and solid line is SE. (**D** to **F**) Thirty-hour continuous measurements for (D) solar intensity and temperatures of SE, BE, and ambient air; (E) relative humidity (RH) and dew point; and (F) the cooling power (P_{Cool}) of SE and BE. The heating power is generated by the power supply output when the sample temperature matches ambient air.

radiation (higher P_{rad}) than the SE. Hence, raising the sample temperature effectively boosts P_{rad} in the BE, making this emitter more suitable for cooling objects that are warmer than ambient air. In experimental results, BE exhibits higher cooling power than that of SE. The average cooling powers of BE and SE are 67.0 and 58.1 W/m², respectively. From morning to afternoon on the second day (6:00 to 14:00), the cooling power difference between two emitters is reduced owing to solar irradiance. In high dew point and high ambient temperature at night on the second day (18:00~), the cooling powers are remarkably decreased regardless of emission features due to abundant water vapor in air (i.e., opaque atmospheric window).

Cooling capability of *J*ET for enclosed space

Heat transfer in open areas mainly occurs by convection, but the mechanism is quite different in an enclosed space with heating sources (*26*). In an automobile parked under the sun, solar radiation enters through the window, while thermal IR radiation cannot escape through it. As a result, the automobile body can heat up to 60 to 82°C when the ambient temperature is only 21°C (*18*), causing heat stroke and hyperthermia in the occupants, especially children (*19*).

The *Janus* thermal radiation characteristic allows the *J*ET to function as a heat channel to draw heat from the enclosure. Because radiation can be maximized by high bottom emissivity (fig. S6, D to F), the *J*ET significantly alters the temperature distribution in the inner region (fig. S6G). Consequently, the *J*ET is highly efficient in dropping temperature from the shielded area by allowing broadband absorption on the bottom side and selective thermal emission from the top through the atmospheric window.

To validate this, we conducted temperature recording experiments using chambers covered with a sample on a rooftop under clear sky with low humidity (Fig. 4A; see Materials and Methods for details). The heater was turned on by DC power supply with a voltage of 7.5 V and a current of 0.105 A, and the heater temperatures were recorded for three samples: C-RC, reverse *J*ET (Rev. *J*ET), and *J*ET. The C-RC is composed of Al plate and thick PDMS (~100 μm) and shows comparable subambient cooling performance with the state-of-the-art ones in daytime (fig. S5J) (*17*). In Rev. *J*ET, the selective emission side faces inside. Figure 4B presents the measured steady-state heater temperature. The *J*ET has exceptional heat dissipation capability compared to the C-RC, as it shows the temperature drop of 3.1°C below C-RC. In addition, this heat release capability lags the heating time when the strong heat source exists in enclosure (fig. S7A). These results indicate that the highest temperature drop exists at *J*ET followed by Rev. *J*ET. The C-RC and Rev. *J*ET are not sufficient regardless of ambient airflow for transferring the inner heat out (Fig. 4C). Although the cooling performance of *J*ET is degraded with h_c and humidity [i.e., when atmospheric transmittance decreases (*24*); Fig. 4D] compared to clear weather as well, the *J*ET always shows better cooling capability than all the other comparison groups. For detailed description on heat transfer simulation and comparison of the heat dissipation, see Materials and Methods and fig. S6.

Figure 4E displays the experimental model mimicking a stationary vehicle in the sun, with Al metal housing. A piece of black leather was placed on the bottom floor as the radiative object atop polystyrene (see Materials and Methods for details; three identical setups were used in each case). The emissivity spectra of the low-emissivity window and leather are shown in fig. S7B. The entire experiment was performed on a rooftop (Fig. 4E, inset). Figure 4F experimentally demonstrates the exceptional cooling performance of *J*ET for enclosed space by comparing two materials (C-RC and Rev. *J*ET), which block the sunlight. This result shows that the *J*ET achieves temperatures of ~4° and 1°C lower than those for the C-RC and Rev. *J*ET, respectively. Repeated measurements for four different days demonstrate the reliability of *J*ET (Fig. 4G). This result also exhibits that the space cooling is still possible in haze day (i.e., day 4), which has average solar power of ~810 W/m² and average humidity of ~44%. The detailed measurement data in different ambient conditions are displayed (fig. S7, C to E). In cloudy day, when the ambient air temperature sustains lower and cooling is avoided, the *J*ET does not provide undesired cooling (fig. S7F).

Last, we note that the material used in this work can be replaced to other polymers with various benefits unless optical properties are neglected. For example, PMMA (polymethyl methacrylate) and PDMS substrate enable large-scale *J*ET with affordability (Supplementary Text, fig. S3, G to K). A transparent top roof measurement result highlights that the larger area of solar transparency remarkably increases the temperature of inner object (fig. S7G). In this context, the increased area of *J*ET is expected to enhance the overall cooling capacity by minimizing solar power and increasing thermal radiation. Furthermore, it is also important to maintain mechanical properties as a car roof. A surface hydrophobicity of *J*ET provides waterproof and self-cleaning effects (fig. S8, A and B). The *J*ET has a low hardness though, the hardness as well as elastic modulus and scratch resistance can be improved by using harder material such as hard PDMS (fig. S8, C to E).

CONCLUSIONS

As a passive strategy to remove heat trapped in enclosed space, the *J*ET shows selective emission on one side to the outer space and broadband absorption on the other side from the enclosure. We first devised an almost-ideal SE with sSPP resonance, composed of 4-μm PDMS layer on Ag-coated micropatterned quartz frame. A 10-μm-thick PDMS layer was coated on the bottom side to facilitate broadband emission (or absorption). Spectral and modal analyses of sSPP resonance provide a guideline for designing SEs using polymer and metal combinations. Strong resonances between the sSPP windows can compensate emissivity loss from low absorption coefficient of the polymer superstrate. For the fabricated *J*ET, the T_{Cool} using the SE was lower than that of the BE. The SE showed a subambient cooling of ~6°C. In 30-hour measurement, the BE exhibited higher P_{Cool} than the SE because of its broadband emission.

Furthermore, we examined the space cooling capability of *J*ET for enclosures. The *J*ET was more effective in drawing heat away as compared to materials with no emissivity and one-directional emissivity. Using *Janus* bidirectional emission characteristics, the *J*ET lowered the temperature of a radiative object inside an enclosure by ~4°C compared to the C-RC in experiments simulating a stationary automobile environment. The significance of the *Janus* for passive heat release from enclosure is illuminating the importance of emissivity of the substrate itself while designing the SE in an interpretive way. With the superior ability to passively cool both surfaces and enclosed spaces, this advanced design leads to comfortability in unconscious and sustainable way, which are critical demands for situation where heat entrance is present and exit is absent (e.g., stationary automobiles).
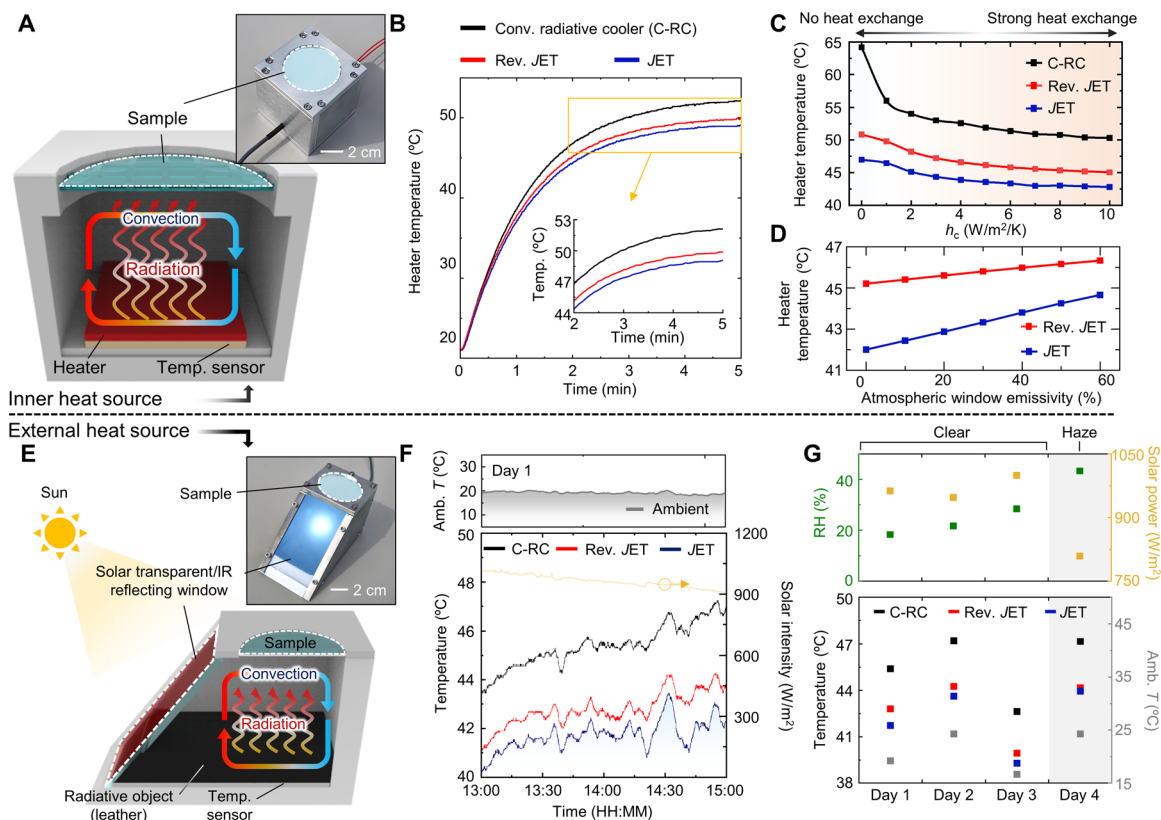
Fig. 4. Demonstration of enclosure cooling using the *Janus* mode of *J*ET. (**A**) Measurement setup using an inner heater. Photo credit: Gil Ju Lee, GIST. (**B**) Measured steady-state heater temperature with C-RC, Rev. *J*ET, and *J*ET. The supplied voltage and current to the heater were fixed as 7.5 V and 0.105 A, respectively, for 5 min. The averaged ambient temperatures were 11.6°, 11.3°, and 11.0°C during the measurements of C-RC, Rev. *J*ET, and *J*ET, respectively. Photo credit: Gil Ju Lee, GIST. (**C**) Simulated heater temperatures considering heat exchange with ambient air for the three radiative coolers. $h_c = 0$ W/m^2 per K refers to no heat exchange between the enclosure and ambient air. The conditions of simulations are as follows: heat flux = 4 W, $T_{amb} = 25$°C, and atmospheric window emissivity in 8- to 13-µm wavelength = 30%. (**D**) Simulated heater temperature depending on the atmospheric window emissivity in 8- to 13-µm wavelength for the three radiative coolers. Lower emissivity indicates more transparent atmospheric window. The simulation parameters are as follows: heat flux = 4 W, $T_{amb} = 25$°C, and $h_c = 4$ W/m^2 per K. The detailed emissivity spectra of coolers and atmospheric window are shown in fig. S6C. (**E**) Schematic setup with heating by external solar radiation in a molded shape of a car. The hole on top of the Al housing is covered by the sample, while the front side is covered by a solar-transparent and IR-reflecting window. (**F**) Temperatures of the radiative object for different groups of cover materials: C-RC (black), Rev. *J*ET (red), and *J*ET (blue). (**G**) Measurements for 4 days with different weather conditions of clear and haze. The weather conditions are estimated in terms of solar power (yellow), RH (green), and ambient air temperature (gray). Black, red, and blue respectively mark the temperatures of three coolers.

MATERIALS AND METHODS
Fabrication of *J*ET
For the etching mask, a 100-nm-thick Cr layer was deposited on a quartz substrate by electron beam evaporation (KVE-E2000, Korea Vacuum Tech Ltd., Korea) at a rate of ~1 Å/s and a pressure of ~10^{-6} torr. Thickness monitoring was performed using a quartz crystal sensor in the vacuum chamber of the evaporator during deposition. To form the *J*ET pattern, a positive photoresist (PR; AZ5214 E, Micro-Chemicals, Germany) was spin-coated at 4000 rpm for 30 s on the quartz substrate with a Cr mask. The sample was then baked on a hot plate at 100°C for 60 s (soft baking). Subsequently, photolithography was performed on the mask of the *J*ET pattern under 365-nm ultraviolet (UV) light for 10 s. Next, the PR was developed by immersion in a developer (AZ-MIF-300, MicroChemicals, Germany). To harden the patterned PR, a post-baking process was conducted on a hot plate at 120°C for 2 min. The sample was then dipped in a Cr wet etchant (CR-7, Transene Company Inc., USA) for 1 min. Next, a ~1.7-µm-thick quartz layer was etched off by a

reactive ion etcher (Oxford Instruments, UK) for 43 min, using CF$_4$ gas [50 standard cubic centimeters per minute (sccm)] at a working pressure of 30 mtorr with a radio frequency power of 100 W. After quartz etching, the Cr hard mask was removed by immersion in a chrome etchant for 15 min. A 100-nm-thick Ag layer was deposited using the electron beam evaporator. Next, PDMS (Sylgard 184, Dow Corning, USA) was mixed with a base:agent ratio of 10:1 and degassed to remove air bubbles, before spin casting on the Ag-coated quartz grating at 8000 rpm for 50 s. Last, the spin-coated sample was cured on a hot plate at 110°C for 2 min.

Numerical simulation and optimization using steady-state energy balance equation
Commercial software (DiffractMOD, RSoft Design Group, Synopsys, USA) using rigorous coupled-wave analysis (RCWA) was exploited to simulate the optical efficiencies, such as the transmittance, reflectance, and absorptivity. The absorption profiles were also studied using this software. In the RCWA, a square grid size of 0.1 nm was

used to numerically calculate the stable optical efficiencies of the *J*ET. Moreover, complex refractive index dispersion was considered to obtain the spectral results. The complex refractive indices of SiO_2 and PDMS were obtained from the literature (*33*, *34*). For the Ag layer, the Drude model was used to achieve material dispersion.

This tool was also used to perform optimization for the *J*ET. Geometrical parameter-dependent emissivity spectra were calculated by sweeping the structural parameters such as duty cycle (*d*), period (*p*), depth (*d*), and thickness (*t*). Using the calculated emissivity spectra, the cooling temperature and cooling power were estimated by MATLAB (MathWorks Inc., USA) based on the thermal equilibrium equation. The detailed cooling power calculations are described in Supplementary Text, Note 3.

Two-dimensional, steady-state simulation of the heat transfer from an enclosure to clear sky

To obtain the local temperature distribution inside the enclosure under steady-state operation, a commercial software (Heat Transfer Module, COMSOL Multiphysics 5.5, USA) was used. Two-dimensional, steady-state thermal energy equation was solved for the enclosure with full consideration of the natural convection inside the inner space due to the buoyancy-driven flow by the heater located at the bottom. The heat conduction through the solid region was implemented by forcing the local velocity zero. In addition, the surface-to-surface radiation exchange based on view factor was also included in the model. For the inner surface, only the heater emits, and the sidewall was assumed to be perfectly reflective. In all computations, the emissivity spectra of C-RC, Rev. *J*ET, and *J*ET shown in fig. S6B were used. For the outer surface, the solar irradiation and the atmospheric emission were considered. The sky transmission in atmospheric window was considered by modeling the ambient emissivity in the wavelength region from 8 to 13 μm (*35*). The detailed atmospheric window spectra in the simulations are shown in fig. S6C. Last, the natural convection between the enclosure outer surface and the ambient air was taken into consideration as the convective boundary condition at the wall.

Spectral and structural characterization

The emissivity was characterized by measuring the reflectance spectra of the *J*ET with a Fourier transform IR (FTIR) spectrometer (VERTEX 70v, Bruker, USA) with Au-coated integrating sphere. Because the IR ray cannot pass through even a thin Ag layer, the emissivity was derived from the measured reflectance spectra. SEM (S-4700, Hitachi Hi-Tech, Japan) was used to observe microstructures in the *J*ET. The mechanical properties were measured by nanoscratch resistance measurement (NST, Anton Paar) with diamond stylus.

Outdoor measurement for surface cooling performances

Adhesive temperature sensors (ST-50, RKC Instrument Inc., Japan) were laminated on the back surface of the samples and then connected to a data logger (RDXL6SD, Omega Engineering, USA). An adhesive polyimide heater was attached to an Ag plate, and the plate was subsequently attached to the back surface of samples. Samples with the attached sensor and heater were placed on polystyrene blocks. To prevent heating of ambient air sensor (RTD-805, Omega Engineering, USA) by solar spectrum, the ambient air sensor was inserted into an Al box with airflow (fig. S5, A and B). A pyranometer (CMP, Kipp & Zonen, The Netherlands) was placed next to the

measurement setup to record the direct and diffuse solar irradiance in daytime. The measurement data in Fig. 3B were performed in four different days: day 1, 11 January; day 2, 16 January; day 3, 26 January; and day 4, 23 January.

For cooling power measurement, DC power supplies (TPT20-10, Toyotech, Korea) were used for the heaters (KHLVA-101/10-P, Omega Engineering, USA). The serial communication of a personal computer with the DC power supply, heater, and temperature logger enabled a closed-loop feedback to measure the cooling power. To eliminate the parasitic resistances in wires connected to heater, we measured the resistances of wires (~4.4 ohms) by multimeter and measured cooling powers considering the voltage drops in the wires.

Outdoor measurements for space cooling with internal and external heat sources

An Al housing structure was used as housing for the space cooling experiment with internal heat source. The housing was composed of Al frame with a thickness of 7.5 mm. The length, width, and height of the housing were 70, 70, and 75 mm, respectively. The outside of the housing was covered by polystyrene blocks to reduce the heat dissipation by ambient air. The inner side of Al housing retains the heat radiated from the heater. A 1-cm-thick polystyrene block was placed on the floor of the housing to minimize conductive heat loss. The polyimide heater (KHLVA-101/10-P, Omega Engineering, USA) integrated with the temperature sensor (RTD sensor with 1/3DIN class, TSTEC, Korea) was attached on top of the polystyrene block. This temperature sensor has 0.1°C tolerance. The temperature sensor was connected to a data logger (GL840, Graphtec Corporation, Japan). To maximize the emissivity from the heater, a commercial BE (Metal Velvet Adhesive Foil, Acktar, Germany) was placed on the heater. The ambient air temperature near the measurement setup was recorded by an air temperature resistance sensor (RTD-805, Omega Engineering, USA). DC power supplies (TPT20-10, TOYOtech, Korea) were used to power the heaters.

To simulate a stationary automobile with an external heat source (i.e., the sun), Al molds were produced by mechanical machining, with a length, width, and height of 130, 65, and 75 mm, respectively. The wall thickness is 7.5 mm. As a solar-transparent and IR-reflecting glass, an indium tin oxide (ITO)–coated quartz plate was used to mimic the low-emissivity window found in real automobiles. To minimize conductive heat loss, a polystyrene block was placed on the bottom floor inside and covered with black-colored leather atop an adhesive temperature sensor (RTD sensor with 1/3DIN class, TSTEC, Korea). The Al frame reflects most of the solar spectrum and thermal waves radiated from the leather. The temperature sensor was connected to a data logger (GL840, Graphtec Corporation, Japan). The air temperature sensor was used for measuring the ambient air temperature near the measurement setup (RTD-805, Omega Engineering, USA). The solar spectrum intensity was measured with a pyranometer (CMP, Kipp & Zonen, The Netherlands). The used temperature sensors have reliable accuracies in hot and cold objects (fig. S5, C to E). The repeated measurements in Fig. 4 were conducted for four different days for reliability: day 1, 20 March; day 2, 22 March; day 3, 23 March; and day 4, 21 March.

SUPPLEMENTARY MATERIALS

Supplementary material for this article is available at http://advances.sciencemag.org/cgi/content/full/6/36/eabb1906/DC1

REFERENCES AND NOTES

1. B. Bhatia, A. Leroy, Y. Shen, L. Zhao, M. Gianello, D. Li, T. Gu, J. Hu, M. Soljačić, E. N. Wang, Passive directional sub-ambient daytime radiative cooling. *Nat. Commun.* **9**, 5001 (2018).
2. International Energy Agency, *Global Energy & CO2 Status Report* (International Energy Agency, 2019).
3. International Energy Agency, *Cooling—Tracking Clean Energy Process* (International Energy Agency, 2019); www.Iea.org/tcep/buildings/cooling [last accessed 16 Oct. 2019].
4. N. N. Shi, C.-C. Tsai, F. Camino, G. D. Bernard, N. Yu, R. Wehner, Keeping cool: Enhanced optical reflection and radiative heat dissipation in Saharan silver ants. *Science* **349**, 298–301 (2015).
5. H.-Y. Chan, S. B. Riffat, J. Zhu, Review of passive solar heating and cooling technologies. *Rev. Sustain. Energy Rev.* **14**, 781–789 (2010).
6. G. Smith, A. Gentle, Radiative cooling: Energy savings from the sky. *Nat. Energy* **2**, 17412 (2017).
7. A. P. Raman, M. A. Anoma, L. Zhu, E. Rephaeli, S. Fan, Passive radiative cooling below ambient air temperature under direct sunlight. *Nature* **515**, 540–544 (2014).
8. Y. Zhai, Y. Ma, S. N. David, D. Zhao, R. Lou, G. Tan, R. Yang, X. Yin, Scalable-manufactured randomized glass-polymer hybrid metamaterial for daytime radiative cooling. *Science* **355**, 1062–1066 (2017).
9. J. Mandal, Y. Fu, A. C. Overvig, M. Jia, K. Sun, N. N. Shi, H. Zhou, X. Xiao, N. Yu, Y. Yang, Hierarchically porous polymer coatings for highly efficient passive daytime radiative cooling. *Science* **362**, 315–319 (2018).
10. T. Li, Y. Zhai, S. He, W. Gan, Z. Wei, M. Heidarinejad, D. Dalgo, R. Mi, X. Zhao, J. Song, J. Dai, C. Chen, A. Aili, A. Vellore, A. Martini, R. Yang, J. Srebric, X. Yin, L. Hu, A radiative cooling structural material. *Science* **364**, 760–763 (2019).
11. G. J. Lee, Y. J. Kim, H. M. Kim, Y. J. Yoo, Y. M. Song, Colored, daytime radiative coolers with thin-film resonators for aesthetic purposes. *Adv. Opt. Mater.* **6**, 1800707 (2018).
12. S. H. Choi, S.-W. Kim, Z. Ku, M. A. Visbal-Onufrak, S.-R. Kim, K.-H. Choi, H. Ko, W. Choi, A. M. Urbas, T.-W. Goo, C. K. Kim, Anderson light localization in biological nanostructures of native silk. *Nat. Commun.* **9**, 452 (2018).
13. Z. Chen, L. Zhu, A. P. Raman, S. Fan, Radiative cooling to deep sub-freezing temperatures through a 24-h day–night cycle. *Nat. Commun.* **7**, 13729 (2016).
14. J.-l. Kou, Z. Jurado, Z. Chen, S. Fan, A. J. Minnich, Daytime radiative cooling using near-black infrared emitters. *ACS Photonics* **4**, 626–630 (2017).
15. L. Zhou, H. Song, J. Liang, M. Singer, M. Zhou, E. Stegenburgs, N. Zhang, C. Xu, T. Ng, Z. Yu, B. Ooi, Q. Gan, A polydimethylsiloxane-coated metal structure for all-day radiative cooling. *Nat. Sustain.* **2**, 718–724 (2019).
16. P.-C. Hsu, C. Liu, A. Y. Song, Z. Zhang, Y. Peng, J. Xie, K. Liu, C.-L. Wu, P. B. Catrysse, L. Cai, S. Zhai, A. Majumdar, S. Fan, Y. Cui, A dual-mode textile for human body radiative heating and cooling. *Sci. Adv.* **3**, e1700895 (2017).
17. X. A. Zhang, S. Yu, B. Xu, M. Li, Z. Peng, Y. Wang, S. Deng, X. Wu, Z. Wu, M. Ouyang, Y. Wang, Dynamic gating of infrared radiation in a textile. *Science* **363**, 619–623 (2017).
18. A. Grundstein, V. Meentemeyer, J. Dowd, Maximum vehicle cabin temperatures under different meteorological conditions. *Int. J. Biometeorol.* **53**, 255–261 (2009).
19. H. Krous, J. Nadeau, R. Fukumoto, B. Blackbourne, R. Byard, Environmental hyperthermic infant and early childhood death: Circumstances, pathologic changes, and manner of death. *Am. J. Forensic Med. Pathol.* **22**, 374–382 (2001).
20. M. M. Hossain, B. Jia, M. Gu, A metamaterial emitter for highly efficient radiative cooling. *Adv. Opt. Mater.* **3**, 1047–1051 (2015).
21. C. Zou, G. Ren, M. M. Hossain, S. Nirantar, W. Withayachumnankul, T. Ahmed, M. Bhaskaran, S. Sriram, M. Gu, C. Fumeaux, Metal-loaded dielectric resonator metasurfaces for radiative cooling. *Adv. Opt. Mater.* **5**, 1700460 (2017).
22. M. M. Hossain, M. Gu, Radiative cooling: Principles, progress, and potentials. *Adv. Sci.* **3**, 1500360 (2016).
23. M. Zeyghami, D. Y. Goswami, E. Stefanakos, A review of clear sky radiative cooling developments and applications in renewable power systems and passive building cooling. *Sol. Energy Mater. Sol. Cells* **178**, 115–128 (2018).
24. D. Zhao, A. Aili, Y. Zhau, S. Xu, X. Yin, R. Yang, Radiative sky cooling: Fundamental principles, materials, and applications. *Appl. Phys. Rev.* **6**, 021306 (2019).
25. Z. Chen, L. Zhu, W. Li, S. Fan, Simultaneously and synergistically harvest energy from the sun and outer space. *Joule* **3**, 101–110 (2019).
26. A. Yücel, S. Acharya, M. L. Williams, Natural convection and radiation in a square enclosure. *Num. Heat Transf. Part A* **15**, 261–278 (1989).
27. D. Cai, A. Neyer, R. Kuckuk, H. M. Heise, Raman, mid-infrared, near-infrared and ultraviolet–visible spectroscopy of PDMS silicone rubber for characterization of polymer optical waveguide materials. *J. Mol. Struct.* **976**, 274–281 (2010).
28. https://refractiveindex.info/?shelf=organic&book=polydimethylsiloxane&page=Query-IR [last accessed 16 October 2019].
29. https://refractiveindex.info/?shelf=organic&book=polydimethylsiloxane&page=Query-NIR [last accessed 16 October 2019].
30. A. Ghanekar, M. Ricci, Y. Tian, O. Gregory, Y. Zheng, Dynamic optical response of SU-8 upon UV treatment. *Opt. Mater. Express* **8**, 2017–2025 (2018).
31. https://refractiveindex.info/?shelf=organic&book=poly%28methyl_methacrylate%29&page=Tsuda-BB [last accessed 16 October 2019].
32. A. Aili, Z. Y. Wei, Y. Z. Chen, D. L. Zhao, R. G. Yang, X. B. Yin, Selection of polymers with functional groups for daytime radiative cooling. *Mater. Today Phys.* **10**, 100127 (2019).
33. R. Kitamura, L. Pilon, M. Jonasz, Optical constants of silica glass from extreme ultraviolet to far infrared at near room temperature. *Appl. Optics* **46**, 8118–8133 (2007).
34. A. Srinivasan, B. Czapla, J. Mayo, A. Narayanaswamy, Infrared dielectric function of polydimethylsiloxane and selective emission behavior. *Appl. Phys. Lett.* **109**, 061905 (2016).
35. https://doc.comsol.com/5.5/doc/com.comsol.help.heat/HeatTransferModuleUsersGuide.pdf [last accessed 08 Febuary 2020].
36. Z. Gao, L. Wu, F. Gao, Y. Luo, B. Zhang, Spoof plasmonics: From metamaterial concept to topological description. *Adv. Mater.* **30**, e1706683 (2018).
37. A new software tool for computing Earth's atmospheric transmission of near-and far-infrared radiation (1992); http://www.gemini.edu/?q=node/10789 [accessed 2 October 2019].
38. J. Yoon, S. Jo, I. S. Chun, I. Jung, H.-S. Kim, M. Meitl, E. Menard, X. Li, J. J. Coleman, U. Paik, J. A. Rogers, GaAs photovoltaics and optoelectronics using releasable multilayer epitaxial assemblies. *Nature* **465**, 329–333 (2010).
39. S. H. Ahn, L. J. Guo, Large-area roll-to-roll and roll-to-plate nanoimprint lithography: A step toward high-throughput application of continuous nanoimprinting. *ACS Nano* **3**, 2304–2310 (2009).

Science Advances

A *Janus* emitter for passive heat release from enclosures

Se-Yeon Heo, Gil Ju Lee, Do Hyeon Kim, Yeong Jae Kim, Satoshi Ishii, Min Seok Kim, Tae Joon Seok, Bong Jae Lee, Heon Lee and Young Min Song

ARTICLE TOOLS	http://advances.sciencemag.org/content/6/36/eabb1906
SUPPLEMENTARY MATERIALS	http://advances.sciencemag.org/content/suppl/2020/08/31/6.36.eabb1906.DC1
REFERENCES	This article cites 32 articles, 6 of which you can access for free http://advances.sciencemag.org/content/6/36/eabb1906#BIBL
PERMISSIONS	http://www.sciencemag.org/help/reprints-and-permissions

Use of this article is subject to the Terms of Service